

# Global-scale surface spectral variations on Titan seen from Cassini/VIMS

Jason W. Barnes<sup>a,\*</sup>, Robert H. Brown<sup>a</sup>, Laurence Soderblom<sup>b</sup>, Bonnie J. Buratti<sup>c</sup>,  
Christophe Sotin<sup>d</sup>, Sebastien Rodriguez<sup>d</sup>, Stephane Le Mouèlic<sup>d</sup>, Kevin H. Baines<sup>c</sup>, Roger Clark<sup>e</sup>,  
Phil Nicholson<sup>f</sup>

<sup>a</sup> Department of Planetary Sciences, University of Arizona, Lunar and Planetary Laboratory, 1629 E. University Blvd., Tucson, AZ 85721-0092, USA

<sup>b</sup> United States Geological Survey, 2255 N. Gemini Drive, Flagstaff, AZ 86001, USA

<sup>c</sup> Jet Propulsion Laboratory, Caltech, 4800 Oak Grove Drive, Pasadena, CA 91109-8099, USA

<sup>d</sup> Laboratoire de Planétologie et Géodynamique, Faculté des Sciences, B.P. 92208, 2 rue de la Houssinière, 44072 Nantes Cedex 3, France

<sup>e</sup> United States Geological Survey, Mail Stop 964, Box 25046, Denver Federal Center, Denver, CO 80225, USA

<sup>f</sup> Department of Astronomy, Cornell University, 418 Space Sciences Building, Ithaca, NY 14853, USA

Received 5 June 2006; revised 18 August 2006

Available online 24 October 2006

## Abstract

We present global-scale maps of Titan from the Visual and Infrared Mapping Spectrometer (VIMS) instrument on *Cassini*. We map at 64 near-infrared wavelengths simultaneously, covering the atmospheric windows at 0.94, 1.08, 1.28, 1.6, 2.0, 2.8, and 5  $\mu\text{m}$  with a typical resolution of 50 km/pixel or a typical total integration time of 1 s. Our maps have five to ten times the resolution of ground-based maps, better spectral resolution across most windows, coverage in multiple atmospheric windows, and represent the first spatially resolved maps of Titan at 5  $\mu\text{m}$ . The VIMS maps provide context and surface spectral information in support of other *Cassini* instruments. We note a strong latitudinal dependence in the spectral character of Titan's surface, and partition the surface into 9 spectral units that we describe in terms of spectral and spatial characteristics.

© 2006 Elsevier Inc. All rights reserved.

**Keywords:** Titan

## 1. Introductory remarks

Though *Voyager 1* detected Titan's surface in retrospect (Richardson et al., 2004), Smith et al. (1996) were first to map the surface, at 0.94 and 1.08  $\mu\text{m}$ , using the *Hubble Space Telescope*. Since then, maps of Titan produced from ground-based adaptive-optics telescopes have been published using data at 1.08  $\mu\text{m}$  (Gendron et al., 2004; Coustenis et al., 2005), 1.28  $\mu\text{m}$  (Coustenis et al., 2001, 2005; Gendron et al., 2004), 1.6  $\mu\text{m}$  (Coustenis et al., 2001, 2005; Roe et al., 2004), and 2  $\mu\text{m}$  (Combes et al., 1997; Gendron et al., 2004; Gibbard et al., 2004; Coustenis et al., 2005). Gibbard et al. (1999) used speckle techniques at 2.1  $\mu\text{m}$  to achieve a similar effect. Meier et al. (2000) used NICMOS to map Titan at 1.08, 1.64, and 2  $\mu\text{m}$ .

The Visual and Infrared Mapping Spectrometer instrument (VIMS) on-board the *Cassini* spacecraft is a slit-scanning visible (0.30–1.05  $\mu\text{m}$ ) spectrometer, the VIS channel (Capaccioni et al., 1998), acting as a single instrument with a spot-scanning near-infrared (0.88–5.1  $\mu\text{m}$ ) spectrometer, the IR channel (Brown et al., 2004). At Titan, VIMS obtains high spatial resolution (down to 250 m/pixel, depending on the range to Titan's surface) spectral mapping of the surface in each atmospheric window simultaneously. As the atmospheric windows fall primarily within the range of the IR channel, we use data from the IR channel exclusively for the present work. VIMS is proving to be a most capable tool for Titan exploration (Sotin et al., 2005).

Though large-scale albedo variations across Titan were detected by Lemmon et al. (1993) and Griffith (1993), reliable detection of variations in spectral signature across Titan were first seen by VIMS (McCord et al., 2006). Determination of surface composition has proven difficult through the at-

\* Corresponding author.

E-mail addresses: [jbarnes@lpl.arizona.edu](mailto:jbarnes@lpl.arizona.edu) (J.W. Barnes), [rhb@lpl.arizona.edu](mailto:rhb@lpl.arizona.edu) (R.H. Brown).

atmospheric absorption windows; current best-fit identifications indicate dirty water–ice (Griffith, 1993; Coustenis et al., 1995; McCord et al., 2006). We hope to improve the composition determinations once we can accurately compensate for Titan’s atmospheric scattering and absorption.

From *Cassini*, the Imaging Science Subsystem (ISS) obtained very high spatial resolution (typically ~few km/pixel) maps of Titan at 0.938  $\mu\text{m}$  over the course of the first few flybys (Porco et al., 2005). Jaumann et al. (2006) published high-resolution VIMS regional mosaics of Titan at 2.0  $\mu\text{m}$ . As of this writing, maps from two synthetic aperture RADAR strips have been published (Elachi et al., 2005, 2006).

In this paper we present atmospherically uncorrected 64-color maps of Titan obtained by VIMS during *Cassini*’s T8 and T9 flybys. These maps represent an improvement over pre-*Cassini* maps with close to an order of magnitude higher spatial resolution, greater coverage with data in seven infrared spectral windows taken simultaneously, and improved spectral resolution across most windows. These VIMS maps complement the higher-spatial-resolution ISS and VIMS maps previously published (Porco et al., 2005; Sotin et al., 2005; Jaumann et al., 2006) and also complement the high-resolution but patchy longer-wavelength RADAR data (Elachi et al., 2005, 2006). We explore the spatially resolved surface spectral inhomogeneities as revealed by the maps and talk about the implications our results have for the processes that shape Titan’s surface and for future mission planning.

The *Cassini* mission is ongoing, as are efforts to understand and correct for the effects of Titan’s atmosphere on VIMS’ surface spectra. *Cassini*’s primary mission continues until 2008, and its first extended mission lasts until 2010. On future flybys VIMS will both expand its coverage area and obtain higher resolution, improved signal-to-noise, and different phase angle observations in those areas previously imaged. Although techniques for atmospheric compensation are progressing, meaningful correction remains realistically years away. Hence the present work is intended to be a scientifically useful reference for comparison with observations from other ground- and space-based instruments, but represents only a step in mining the VIMS dataset for Titan’s surface spectral diversity.

## 2. Observations

During *Cassini*’s T8 (2005 October 28) and T9 (2005 December 26) flybys of Titan, VIMS obtained 193 spectral mapping cubes of Titan, as detailed in Table 1. These two flybys were chosen in particular because they were taken at low phase angle, because they both have consistent and relatively high (~45 km/pixel minimum) spatial resolution, because the total coverage they provide spans VIMS’ total coverage area, because they are nearly free of clouds, and because the incidence and emission angles near the limb where the two flybys’ observations overlap facilitates mosaicing by minimizing discontinuities at the seams.

Due to constraints imposed by *Cassini*’s orbital tour design, during each flyby thus far VIMS has observed roughly either Titan’s sub-saturnian hemisphere or the hemisphere centered

around 140° W 0° N. The former are called Fentzal–Aztlan passes after the distinctive sideways H-shaped dark area thousands of km long centered near 40° W 10° S. The latter are known as Shikoku passes after the 200-km diameter Great Britain-shaped bright area centered at 165° W 10° N.

T8 is a Shikoku pass. T9 is a Fentzal–Aztlan pass. Though neither flyby’s observations represent extremes in coverage—for instance the Ta coverage extends west of that from T8 and includes the Huygens landing site and T11 extends east of T9—these two flybys do provide a representative sample of VIMS’ Titan coverage. Overlap between the two datasets occurs in a ~30° wide swath centered around 80° west longitude.

We reduce the raw data into  $I/F$  as a function of wavelength for each of the 256 VIMS-IR channels using the standard VIMS pipeline (see Brown et al., 2004, and references therein for specifics about how the VIMS instrument functions):

- I On-board the spacecraft, for each line VIMS observes it measures a background level. For each cube we create a linear fit to the background observations and subtract the linearly interpolated background from each pixel.
- II We begin the automatic pipeline process for the VIMS-IR channel by marking those pixels that have saturated.
- III Next the pipeline employs a despiking algorithm to identify pixels whose flux is dominated by cosmic ray hits. We assign the offending pixels an interpolated value based on a 3-D polynomial fit of the twenty-six nearest neighbor pixels.
- IV We divide through by a spatial flatfield that was taken on the ground before launch at each wavelength.
- V We convert to specific energy ( $I_\lambda$ ) using the instrument’s spectro-radiometric response function  $R(\lambda)$  in photons per analog-to-digital data number (DN) (Brown et al., 2004):

$$I_\lambda = \frac{\text{DN}}{\tau} \times R(\lambda) \times \frac{hc}{\lambda} \times \frac{1}{A\Omega\delta\lambda}, \quad (1)$$

where  $\tau$  is the exposure time in seconds,  $h$  is Plank’s constant,  $c$  is the speed of light,  $\lambda$  is the wavelength of this particular VIMS channel,  $\delta\lambda$  is the size of the wavelength bin for this VIMS channel,  $A$  is the area of the VIMS mirror, and  $\Omega$  is the solid angle subtended by a pixel in steradians.

- VI We then divide by a solar spectrum (Thekekar, 1973) with the solar flux at the instantaneous Sun–target distance,  $R_{\odot-T}$  to arrive at  $I/F$ :

$$\frac{I}{F} = \frac{I_\lambda}{F_{1,\lambda} \left( \frac{R_{\odot-\oplus}}{R_{\odot-T}} \right)^2}, \quad (2)$$

where  $F_{1,\lambda}$  is the specific solar flux at 1 astronomical unit ( $R_{\odot-\oplus}$ ).

- VII Using SPICE (Acton, 1999) data provided by JPL, we calculate the latitude, longitude,  $x$ - and  $y$ -direction resolution, phase angle, incidence angle, emission angle, and north azimuth of every point individually. These data are stored in the cube backplane. Since the VIMS-IR is a spot-scanner (Brown et al., 2004), we are able to thus compensate for spacecraft pointing changes during an exposure.

Table 1  
Summary of observations

Sequence	Cube	Dims	Best res. (km)	Exp. times (ms)	Notes
<i>T8</i>					
017_TI_MIDIRMAP008_CIRS	11	48 × 36	210	10 × 80 1 × 640	Driftscan, smeared
017_TI_MONITOR001_ISS	5	64 × 64	80	5 × 80	Global
017_TI_MEDRES001_PRIME	20	64 × 64	50	2 × 40 13 × 80 4 × 160 1 × 240	All Titan at uniform resolution
017_TI_HIRES001_ISS	7	64 × 64	42	3 × 20 4 × 80	Center near Shikoku
<i>T9</i>					
019_TI_NADIRCOMP001_CIRS	10	64 × 64	90	4 × 40 3 × 80 1 × 160 2 × 320	High S/N global
019_TI_MEDRES001_PRIME	23	64 × 64	60	3 × 20 2 × 40 13 × 80 2 × 160 1 × 180 1 × 240 1 × 260	Global– subglobal
019_TI_GBMAPHDAC001_ISS	89 5	12 × 12 64 × 64	19	5 × 40 43 × 80 46 × 320	Teenies
019_TI_HDAC001_UVIS	23	64 × 64	2.7	15 × 80 5 × 160 2 × 320 1 × 640	Approach and high-phase lookback

*Note.* The fourth column represents the best spatial resolution of the sequence, not a median or typical resolution. Not all Titan data are shown for each flyby, only the ones useful for surface studies used in the present work.

### 3. Mapping methods

We store and mosaic the VIMS cubes using a simple cylindrical projection centered around the sub-Saturn point. For each individual cube we map backwards, assigning to each point in a cylindrical map the value of the nearest neighbor pixel in the VIMS cube, within a given radius. We set this maximum distance radius to be one half the diagonal size of the pixel as set in the backplane information, times a margin factor, typically 1.3. The resulting system compensates for gaps between VIMS pixels that can otherwise occur in the cylindrical map. Smaller margin factors inadequately cover the gaps between pixels; larger margin factors affect only the edge pixels, extending them outward.

An automated system takes each VIMS cube and projects it into its own cylindrical map with a resolution in pixels per degree 2.3 times greater than the best spatial resolution in the original cube. VIMS' inherent resolution is 0.0005 milliradians in normal mode and 0.00025 milliradians in hires mode (Brown et al., 2004)—hence the spatial resolution on Titan for each point is a function of the range to Titan at the time those data were taken modified by projection effects on Titan's disk. For each point in the individual maps we calculate a figure of

merit,  $f$ , that we will use when stitching these frames together:

$$f \equiv R_x R_y t^{\frac{1}{2}} \cos^2 i \cos^2 e, \quad (3)$$

where  $R_x$  and  $R_y$  are the spatial resolution of the original VIMS pixel in the sample and line directions respectively,  $t$  is the integration time,  $i$  is the incidence angle, and  $e$  is the emission angle. The expression for  $f$  is one of our invention, and is intended to serve as a quantitative measure of the data quality at each point. The figure of merit expression can be modified depending on the goals of the particular mapping task.

To composite the resulting individual frames, we employ two different methods. For maps useful for morphological interpretation, we create best-spatial-resolution products by mosaicing the individual cylindrical frames together, assigning to each latitude and longitude point in the map the spectrum of the original VIMS pixel with the highest  $f$ . In the case where a pixel is saturated, data from the pixel with the next-highest  $f$  is substituted for just that wavelength channel. Hence we make the best use of sets of observations with different exposure times, taking the high signal-to-noise pixels from the long integration cubes, but substituting in lower S/N data where the long exposure leads to saturation.

Spectral analysis algorithms like principal components projection and cluster analysis are sensitive to noise. The second

map composition method seeks to maximize S/N and minimize pixel-to-pixel variation by coaveraging observations with similar values of  $f$ . Typically we coaverage original VIMS pixels whose  $f$  is within a factor of 2 of one another. Similar to the previous case, saturated pixels are not included in the averages, keeping the results robust.

Maps generated using data obtained during the T8 and T9 Titan encounters are shown in Figs. 1 and 2. To facilitate intercomparison between spectral windows, we also present one representative map from each window, equivalently scaled, in Fig. 3. Each flyby was treated independently, and we joined together the results taking the at each latitude and longitude the  $I/F$  value from the flyby whose map has the greatest figure of merit value,  $f$ . These maps employ spatial sampling of 2 pixels per degree and optimize S/N. We show maps at 64 different wavelengths where the VIMS-IR channel sees Titan's surface in and around the spectral windows at 0.94, 1.08, 1.28, 1.6, 2.0, 2.8, and 5  $\mu\text{m}$ . Each wavelength's image is stretched from zero to an  $I/F$  1.35 times greater than that at the 95th percentile to bring out details in the dimmer images.

#### 4. Descriptions

Not all of the features shown in Figs. 1 and 2 maps are surficial—some are atmospheric contributions. Though during T8 Titan was nearly free of clouds, during T9 Titan had a prominent storm system located at the south pole. The bright (usually off-scale) region in the sub-Saturn hemisphere southward of  $70^\circ\text{S}$  is this cloud deck, which we ignore in this surface-oriented paper. We similarly ignore areas not in direct sunlight, such as the north pole.

At the edges of the spectral transmission windows, where atmospheric species absorb incoming and outgoing light, a smaller fraction of insolation reaches both down the surface and back up to VIMS. Scattering from haze particles then contributes a greater fraction of the detected flux, as can be seen in Figs. 1 and 2.

Titan's atmospheric haze scatters more effectively at shorter wavelengths, and less effectively at longer wavelengths. Hence the atmospheric window least affected by haze is that at 5  $\mu\text{m}$  (Fig. 2, bottom). VIMS measures Titan's overall albedo to be quite low in this window, between 0.017 and 0.10, consistent with earlier ground-based disk-integrated spectra (Noll et al., 1996) (determination of albedos from  $I/F$  in the other spectral windows would require an atmospheric correction). Ground-based adaptive optics systems generally have difficulty viewing Titan at wavelengths longer than  $\sim 2.7\ \mu\text{m}$  due to high thermal background, leaving VIMS' observations as the first resolved maps of Titan in the 5  $\mu\text{m}$  window.

Titan's low 5  $\mu\text{m}$  reflectivity combined with lower solar flux and detector sensitivity make for low signal-to-noise ratios in individual VIMS cubes. The figure-of-merit-based coaveraging scheme described in Section 3 is particularly useful for bringing out signal within the 5  $\mu\text{m}$  window. The 5.091  $\mu\text{m}$  channel has particularly low S/N relative to the other channels, so when coadding all of the 5  $\mu\text{m}$  window into a single image, we use the 15 channels between 4.869 and 5.123  $\mu\text{m}$  excluding 5.091  $\mu\text{m}$ .

Atmospheric contribution is next-lowest in the 2  $\mu\text{m}$  window. Despite the longer wavelength, the surface contribution is low enough at 2.7  $\mu\text{m}$  within double-peaked window for atmospheric scattering to account for a greater fraction of detected flux than at 2  $\mu\text{m}$ . VIMS' achieves its best signal-to-noise ratio in the 2  $\mu\text{m}$  window.

Scattering becomes progressively more important in the shorter-wavelength windows 1.6, 1.28, 1.08, and 0.94  $\mu\text{m}$ . For comparison, *Cassini's* Imaging Science Subsystem (ISS) images Titan at 0.938  $\mu\text{m}$  (Porco et al., 2005), within the 0.94  $\mu\text{m}$  spectral window.

#### 5. Interpretations

To decant the 64 VIMS channels that show Titan's surface into a more manageable set, we use coverages from the peak of each spectral window with two for the double-peaked 2.7  $\mu\text{m}$  window. The 5  $\mu\text{m}$  window shows the greatest color variation relative to the other windows. Therefore we display as much information as possible using three colors by using the 5  $\mu\text{m}$  window as red, 2  $\mu\text{m}$  as green representing overall albedo, and the 1.3  $\mu\text{m}$  window as blue representing most of the remaining color variation. We show Titan composite maps generated from the T8 and T9 flybys using this color scheme, along with orthographic projections, in Figs. 4 and 5.

Fig. 4 uses a 4-pixels-per-degree grid and is designed to optimize spatial resolution (see Section 3). Though for this work memory address limitations inherent to 32-bit computing architecture limits our maximum global spatial sampling to 4 pixels-per-degree, we have recently implemented modifications that allow arbitrarily high resolution, limited only by hard storage space and computation time. VIMS' best spatial resolution obtained to date is  $\sim 1\ \text{km/pixel}$ , thus for future mapping we expect to be able to produce maps nearing 45 pixels-per-degree globally. This type of map is best for photogeological interpretation; as in this work we are concentrating on large-scale spectral differences, we prefer to concentrate on signal-to-noise optimized maps like those in Fig. 5. Titan's geology as seen by VIMS will be discussed separately (Sotin, in preparation).

Figs. 5–7 use coaveraging to improve signal-to-noise. The total integration time for each location is depicted in Fig. 8. They are sampled with 2 pixels-per-degree. Note that the coaveraging scheme intentionally degrades VIMS' spatial resolution in these maps in order to facilitate identification of global-scale spectral units. While Fig. 5 uses the same color scheme as Fig. 4, Figs. 6 and 7 utilize Titan's other 4 atmospheric windows. Specifically, Fig. 6 represents Titan's surface using a color map with 1.6  $\mu\text{m}$  as red, 1.08  $\mu\text{m}$  as green, and 0.94  $\mu\text{m}$  as blue, and Fig. 7 concentrates on the 2.7  $\mu\text{m}$  double-peak by assigning 2.8  $\mu\text{m}$  to be red, 2.7  $\mu\text{m}$  to be green, and 2.00  $\mu\text{m}$  as blue to represent global albedo.

As evidenced in Figs. 5–7, Titan's surface displays a strong latitudinal zonation in spectral character. The area within  $\sim 25^\circ$ – $35^\circ$  of the equator is distinct from that in the mid-latitudes of both hemispheres, and from the area within  $30^\circ$ – $40^\circ$  of the south pole.



Fig. 1. VIMS maps of Titan at 32 wavelengths where the surface can be seen. See also Fig. 2. Wavelength for each image is denoted in the upper-left, stretch applied for each image is in upper right in units of  $I/F$ . These maps are spatially sampled at 2 pixels per degree and maximize S/N (see text).



Fig. 2. VIMS maps of Titan at 32 wavelengths where the surface can be seen. See also Fig. 1. Wavelength for each image is denoted in the upper-left, stretch applied for each image is in upper right in units of  $I/F$ . These maps are spatially sampled at 2 pixels per degree and maximize S/N (see text).

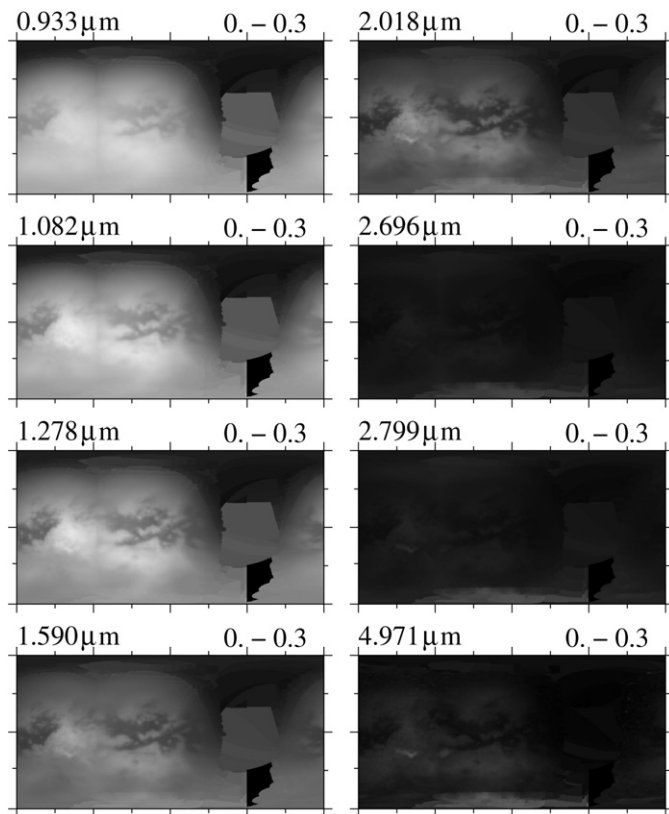


Fig. 3. VIMS maps of Titan within seven of Titan's spectral windows (with two for the 2.8  $\mu\text{m}$  window). Wavelength for each image is denoted in the upper-left. These images all use the same stretch to present the data: 0.0–0.3 in units of  $I/F$ .

In this section we describe the global distribution of spectral units and their rough spectral characteristics; we will present global unit maps and explicit spectra later, in a forthcoming publication. Attempted identification of specific chemical species based on surface spectra is beyond the scope of this work. Readers are directed to McCord et al. (2006) for a first attempt at chemical identification.

### 5.1. Equatorial zone

As was first noted by Porco et al. (2005), the most striking dichotomy near the equator is between dark terrain and bright terrain. VIMS differentiates the bright terrain into Xanadu and non-Xanadu, and the dark terrain into “dark brown” and “dark blue.” We define the equatorial zone to be roughly within  $25^\circ$ – $30^\circ$  of the equator. We present an annotated overview map in Fig. 9 to aid in locating the regions we discuss.

#### 5.1.1. Dark brown

Cassini's RADAR identified expansive seas of longitudinal sand dunes located in areas near Titan's equator (Lorenz et al., 2006). Soderblom (in preparation) first noted that the locations where RADAR sees dunes correlate with areas VIMS sees as dark brown (Fig. 10). These areas broadly correlate with those ISS sees as dark; most of Titan's optically dark areas come out as dark brown spectrally, and we infer that in these areas sand dunes probably predominate. Colors for dark brown terrain are

relatively dark in all atmospheric windows. The margins of dark brown terrain are sharp with all other units that it contacts.

It is not yet clear whether all dark brown areas are necessarily equally dune-covered. In Fig. 10 the subtle linear markings that VIMS sees do not correlate with archetypical, strong ‘cat-scratch’-type dunes in RADAR, but rather with less-contrasting linear features. It may be that in some areas, particularly those farther from the equator such as those shown in Fig. 10, lower sand supplies lead to dunes of lower amplitude.

At the far right edge of the VIMS image in Fig. 10 we catch a few pixels of a higher amplitude dune feature as seen in RADAR—this small glimpse supports the dune/dark brown correlation (Soderblom, in preparation). Larger and higher amplitude VIMS features at the northern end of Fig. 10 may be related to the dunes, but are located off the edge of the T3 RADAR swath (Elachi et al., 2006) such that no intercomparison of the two datasets is possible there. Future VIMS observations on the 2006 October 25 (T20) flyby may supply further insights into the nature of the dark brown unit.

#### 5.1.2. Dark blue

The minority of Titan's equatorial optically dark zones are what Soderblom (in preparation) calls “dark blue”; we show an example of the dark blue unit in Fig. 11. The dark blue spectral unit clings to the eastern margins of equatorial bright terrain; in other words, it lies at the western end of contiguous dark areas, with the exception of the parabolic ejecta of Sinlap crater. This spatial distribution of the dark blue unit could be the result of net sand transport occurring in a west-to-east direction, leaving the westernmost reaches of dark areas bereft of sand. The margins of the dark blue unit are clear and distinct down to a resolution of a few km/pixel.

Extending southeast from Sinlap crater is a parabolically-shaped outcrop of the dark blue spectral unit. Its location and morphology suggest that it was emplaced as part of an ejecta plume blown downwind of the impact site. The persistence of this outcrop of dark blue terrain with unencumbered dunes to its west implies that either the net migration rate of the dunes is very slow, or that Sinlap crater was emplaced relatively recently. The crater's well-preserved structures as seen by RADAR (see Elachi et al., 2006) imply that the latter is more likely the case.

Spectrally, this unit is dark at 1.6, 2.0, and 5.0  $\mu\text{m}$  relative to other Titanian terrain, but moderately reflective at 1.3, 1.08, and 0.94  $\mu\text{m}$  as can be seen in Figs. 5 and 6. Rodriguez et al. (2006) have attributed this behavior to a possible higher fraction of large-grained water-ice, the spectrum of which we show in Fig. 12. Reflectances at 2.7 and 2.8  $\mu\text{m}$  are commensurate with the Rodriguez et al. (2006) interpretation, as are those in the shorter wavelength windows. McCord et al. (2006) argue that none of Titan's terrain can be pure water ice based on the 2.8/2.7  $\mu\text{m}$  band ratio (see Fig. 12).

Though 2.8/2.7  $\mu\text{m}$  band ratios imply that there is no enhancement in water ice in the dark blue material relative to the equatorial bright unit, broad color differences between the 0.94, 1.08 and 1.3  $\mu\text{m}$  spectral windows relative to the 1.6, 2.0, and 5.0  $\mu\text{m}$  windows imply enhanced water ice in the dark blue

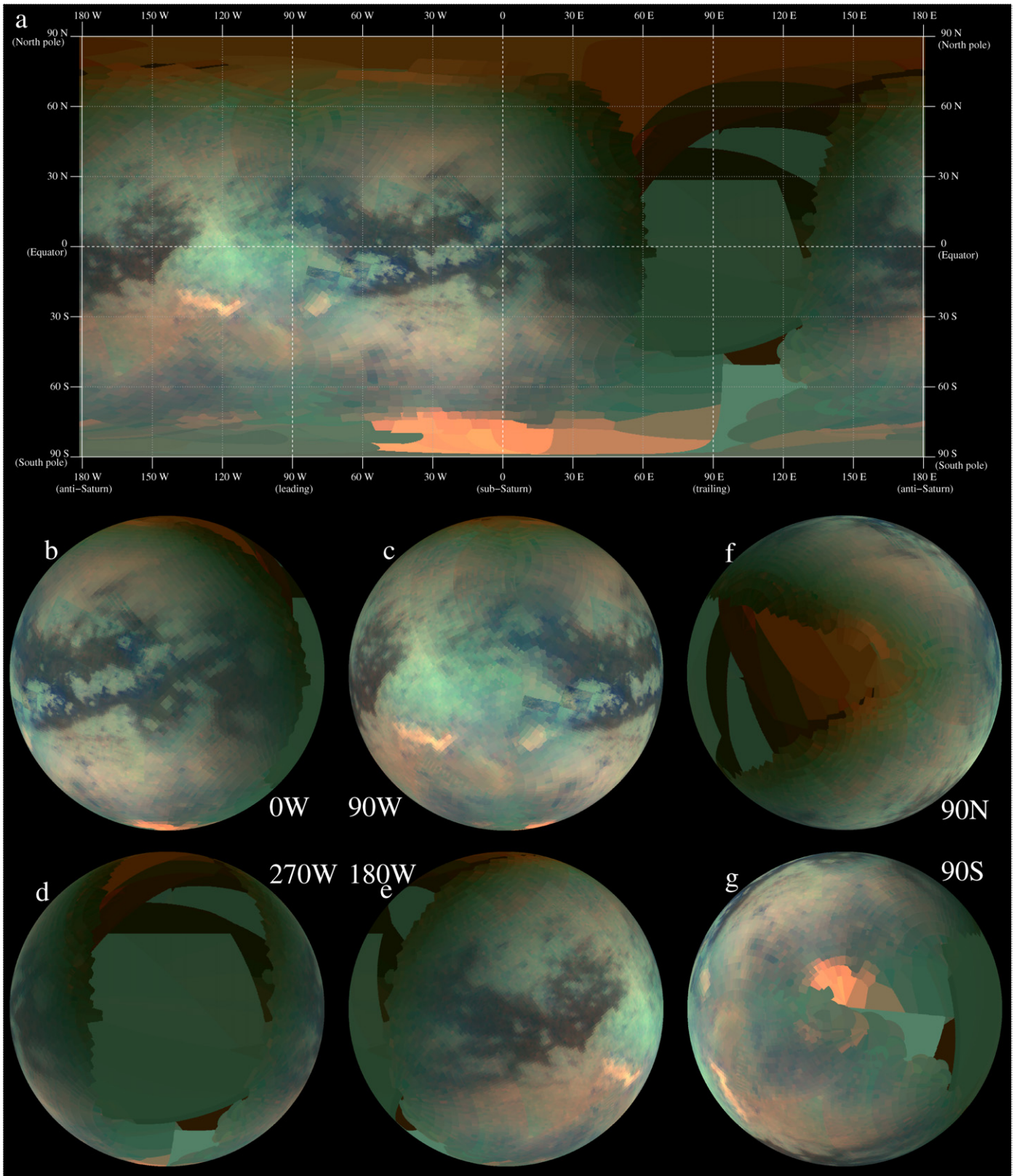


Fig. 4. VIMS map of Titan from T8 and T9, designed for maximum spatial resolution (see text). (a) Simple cylindrical map, (b–f) orthographic projections from above, (b) 0° N 0° W with N at top, (c) 0° N 90° W with N at top, (d) 0° N 270° W with N at top, (e) 0° N 180° W with N at top, (f) 90° N with 0° W at top, (g) 90° S with 90° W N at top. Colors are mapped with 4.8–5.2 μm as red, 2.00 μm as green, and 1.28 μm as blue.

spectral unit compared to dark brown. Note that as dark blue terrain is moderately bright at 0.94 μm, it is identifiable in ISS

0.938 μm imagery as ‘fuzzy,’ and can be differentiated from both dark brown and bright terrains based on this texture.

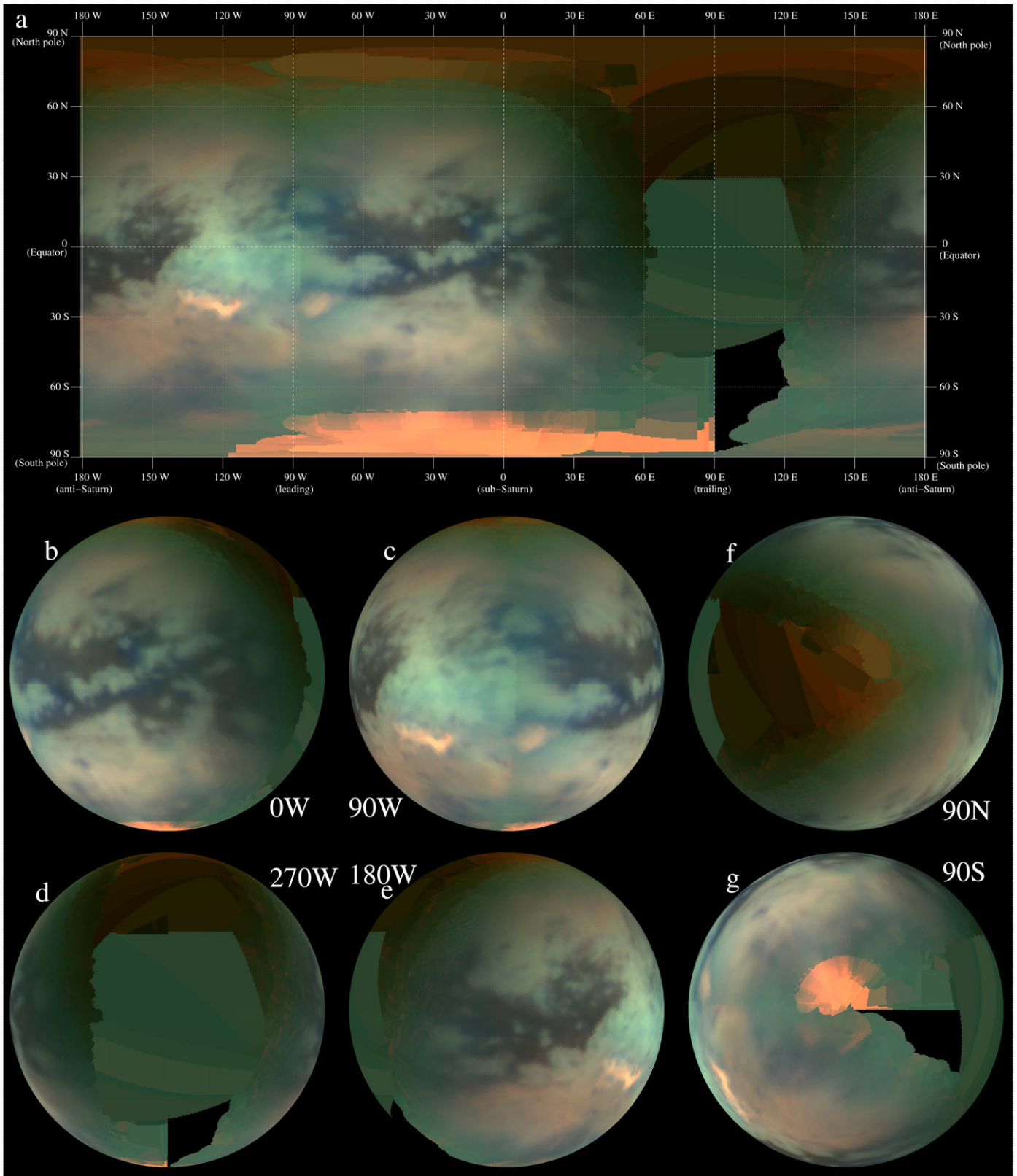


Fig. 5. VIMS map of Titan from T8 and T9, designed for maximum S/N (see text). Projections are as in Fig. 4. Colors are mapped with 4.8–5.2  $\mu\text{m}$  as red, 2.00  $\mu\text{m}$  as green, and 1.28  $\mu\text{m}$  as blue.

*Huygens* landed on dark blue terrain (Rodríguez et al., 2006, called “unit 1” therein). Since dark blue terrain comprises less than 10% of the equatorial dark regions which themselves

cover perhaps a quarter of Titan’s surface area (precise values await coverage of Titan’s trailing hemisphere), the precise *Huygens* landing site is not directly representative of most

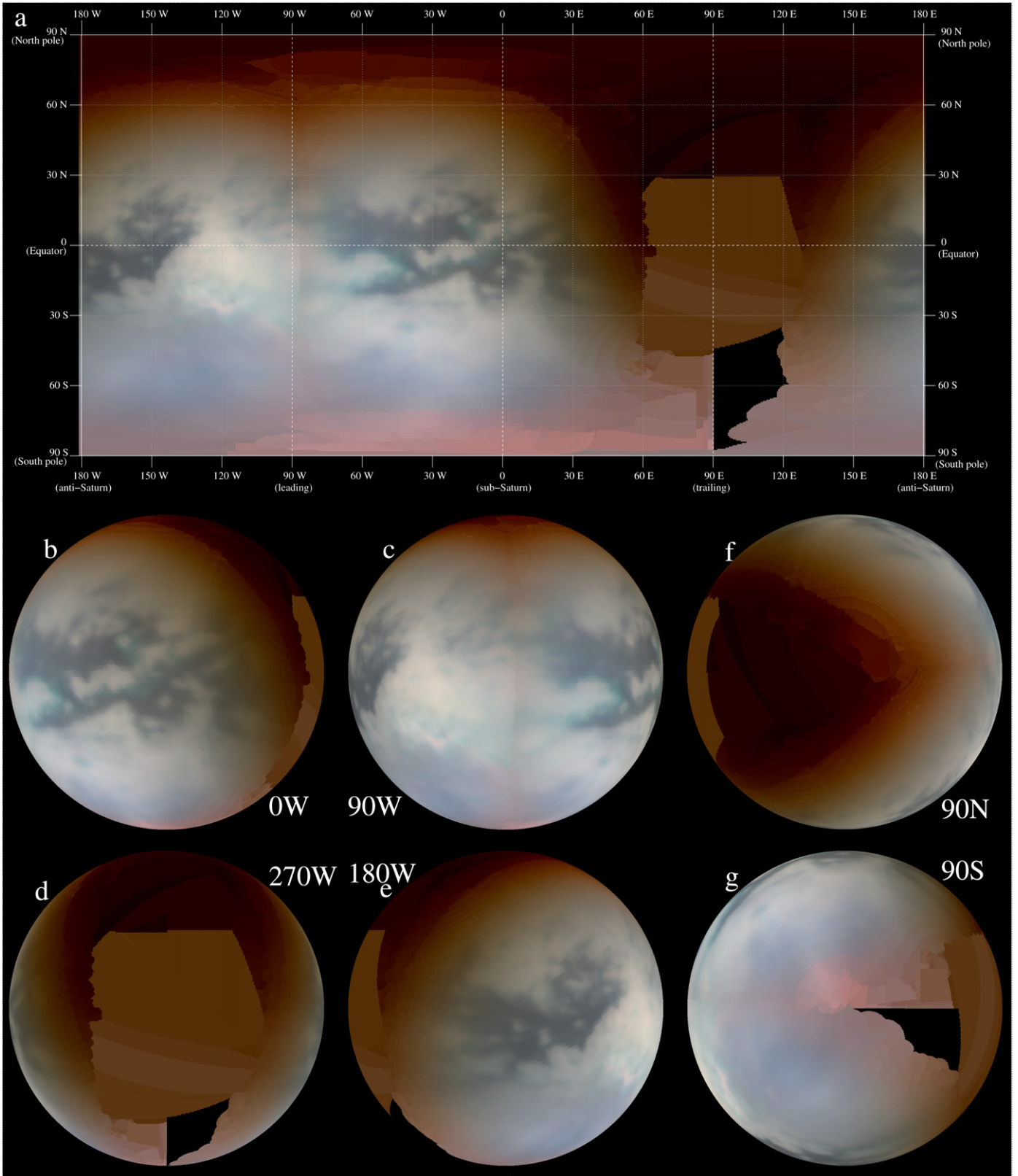


Fig. 6. VIMS map of Titan from T8 and T9, designed for maximum S/N (see text). Projections are as in Fig. 4. Colors are mapped with 1.6  $\mu\text{m}$  as red, 1.08  $\mu\text{m}$  as green, and 0.94  $\mu\text{m}$  as blue.

of Titan’s surface. Only a few percent of Titan’s total surface area matches the surface spectral signature of the landing site.

### 5.1.3. Xanadu

The large equatorial bright unit Xanadu was first seen from Earth (Smith et al., 1996). VIMS’ contribution reveals that al-

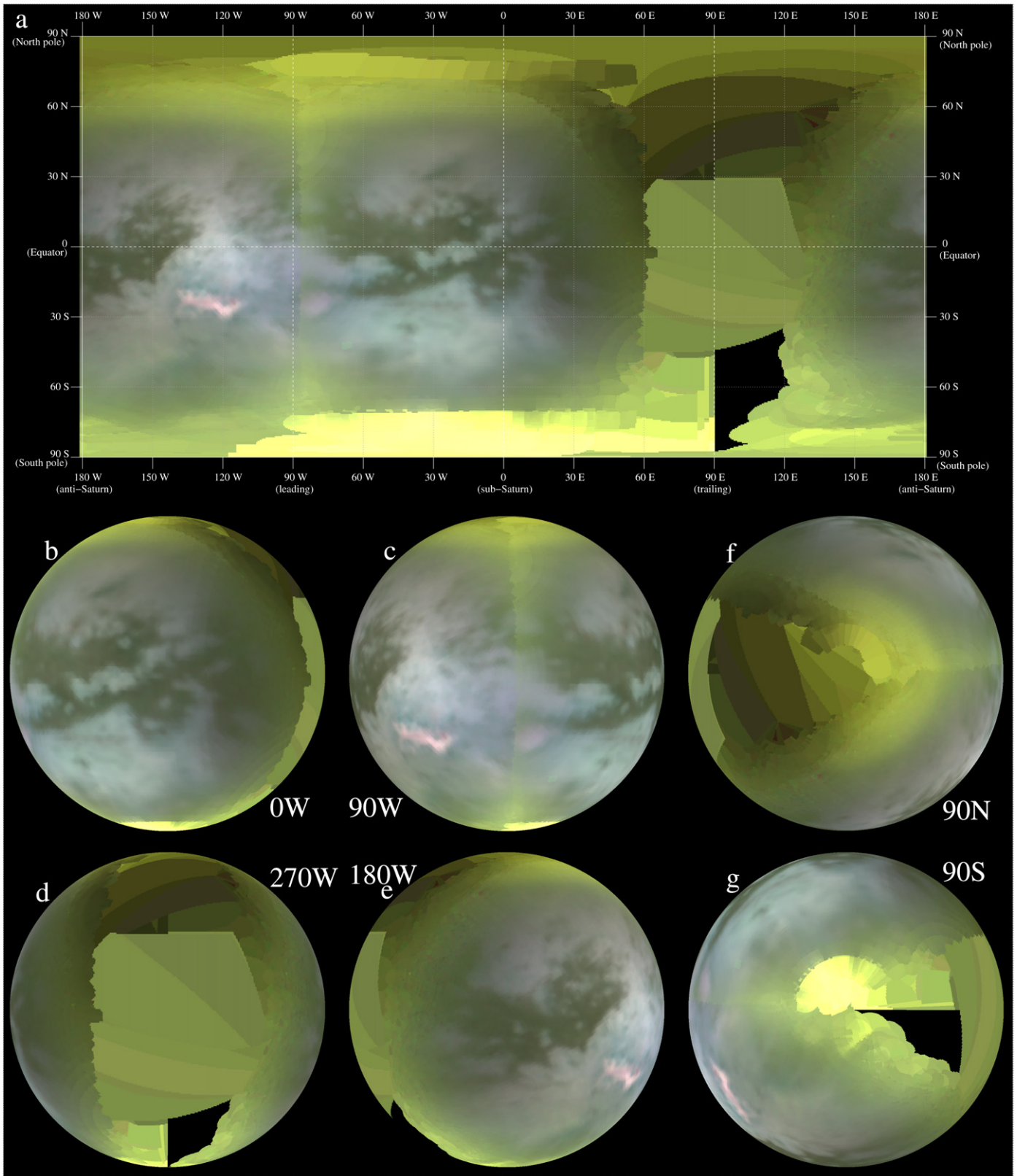


Fig. 7. VIMS map of Titan from T8 and T9, designed for maximum S/N (see text). Projections are as in Fig. 4. Colors are mapped with 2.8  $\mu\text{m}$  as red, 2.7  $\mu\text{m}$  as green, and 2.0  $\mu\text{m}$  as blue.

though Xanadu is bright in all of the shorter atmospheric windows, its reflectivity at 5  $\mu\text{m}$  is less than that of Titan's other large bright areas. In fact, at 5  $\mu\text{m}$  a different bright region,

Tsegihi, is the brightest large-scale feature on Titan's surface (see Section 5.2.1). Xanadu's spectral variations are evident in Fig. 5 where Xanadu appears green and Tsegihi appears

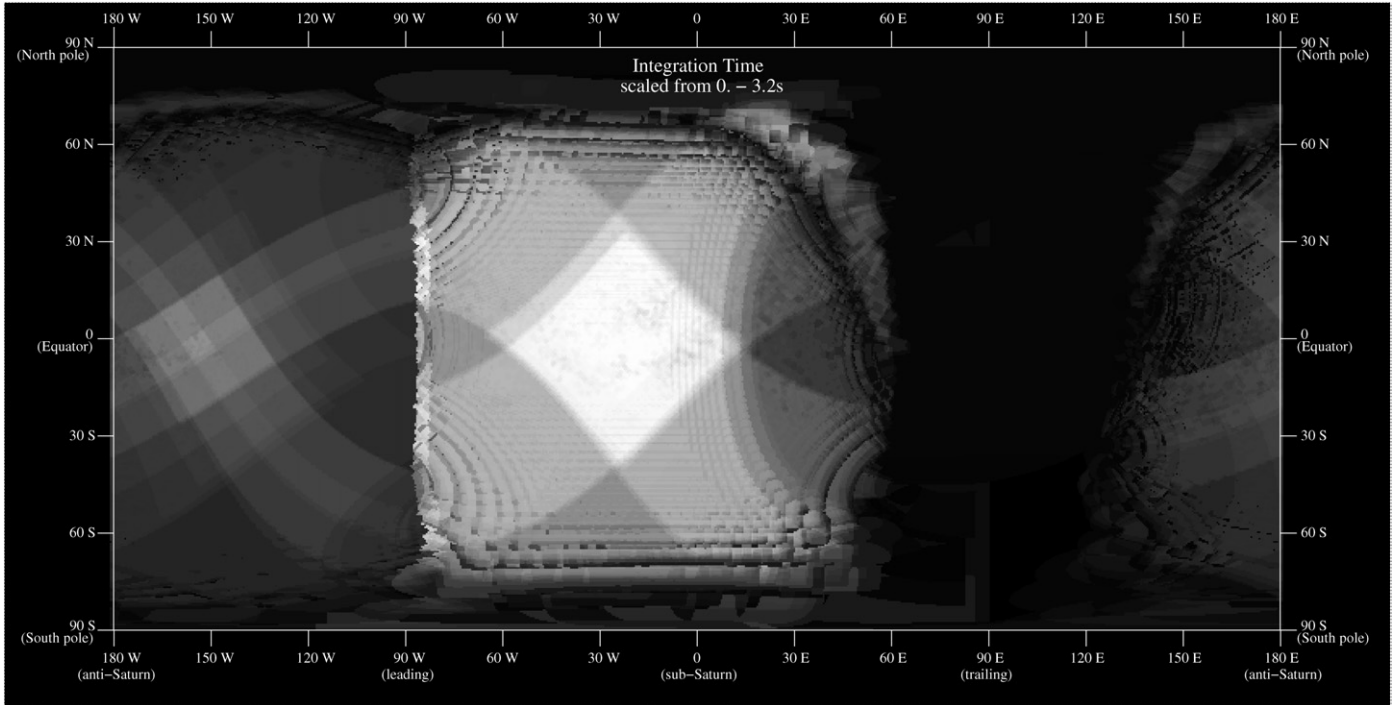


Fig. 8. Total integration time per pixel for the 2-pixel-per-degree coverage maps used in Figs. 1, 2, 5, 6, and 7. Figure is scaled with black as 0 ms integration time, and white at 3200 ms integration time. Median integration time is 1000 ms.

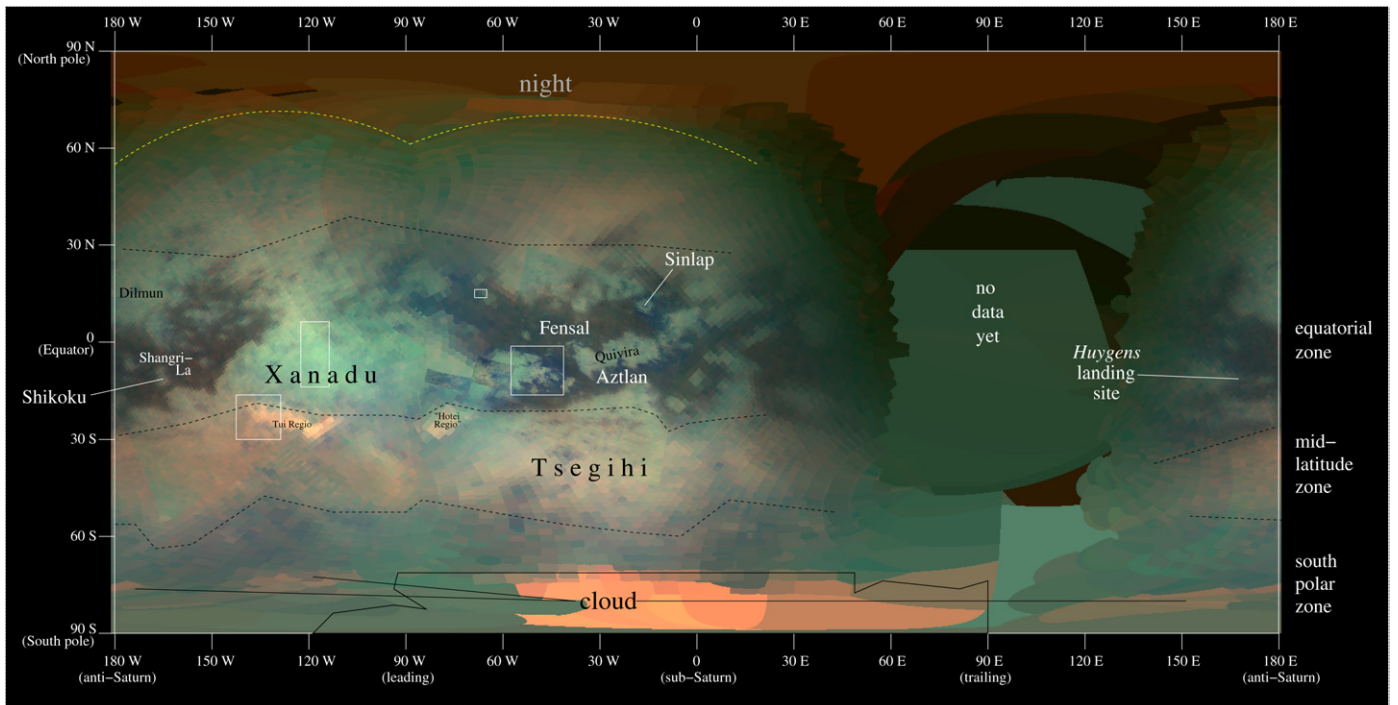


Fig. 9. Cylindrical map from Fig. 4, annotated. Names are all IAU accepted or provisional designations (Owen et al., 2006), with the exception of “Hotei Regio” which we use following Barnes et al. (2005).

peach-colored. Xanadu and the equatorial bright terrain both share a relatively poor reflectivity at 5  $\mu\text{m}$  relative to that of Tsegih'i and the rest of the mid-latitude zone. Both the equatorial and mid-latitude zones are dimmer at 5  $\mu\text{m}$  than they are at 2  $\mu\text{m}$ .

Xanadu’s margins are indistinct, particularly on the eastern edge (though this could be partially due to our poor coverage there). The spectral province of Xanadu does not extend past  $\sim 90^\circ\text{W}$ —the precise eastern boundary has not been identified due to the low resolution and large atmospheric effects for this

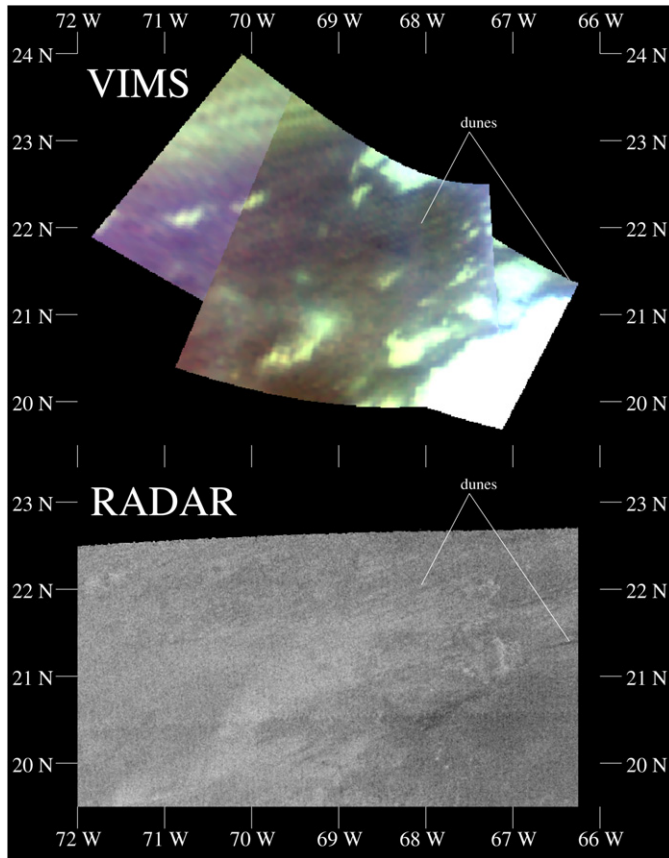


Fig. 10. VIMS T4 (top) and RADAR T3 (bottom) high-resolution views of an area in northwest Fensal containing probable dune features. These are not the classic, high-amplitude cat-scratch-type dunes that RADAR saw closer to the equator (Lorenz et al., 2006), but rather have more subdued appearance. The VIMS image uses 2.8  $\mu\text{m}$  for red instead of 5.0  $\mu\text{m}$  because the relatively short integration time for these cubes (100 ms) combined with the subtlety of the dune modulation render the dunes undetectable in the 5  $\mu\text{m}$  band. The VIMS image has a maximum resolution of 1.3 km/pixel and is sampled at 100 pixels per degree using Lanczos interpolation. We enhanced the contrast in order to bring out the dunes. Blue color in the dark area at the west end of the VIMS is atmospheric scattering—as this cube was taken close to Titan, the geometry varied significantly during the acquisition of each cube and between the two cubes used to generate this image.

longitude over the flybys to date. It is possible that Xanadu has no precise margins, but rather gradually blends in to the surrounding equatorial bright terrain on the east.

We show VIMS best-resolution view of Xanadu so far in Fig. 13. VIMS finds only subtle spectral variations within Xanadu. Numerous sinuous, linear, albedo-dark features are visible in this view. The lineaments could represent tectonic fractures, in which case Xanadu might be interpreted as being young. The shape of the most prominent linear dark feature resembles those of European cycloids (Hoppa et al., 1999). Alternately these dark lines could represent channels such as those seen at the Huygens landing site (Tomasko et al., 2005) and the equatorial bright unit (see below). Under this hypothesis, Xanadu would be relatively old, having stream systems with integrated drainages as opposed to short, stubby networks surrounding inland seas or playa lakes. The scheduled T13 RADAR pass may differentiate between these two possibilities.

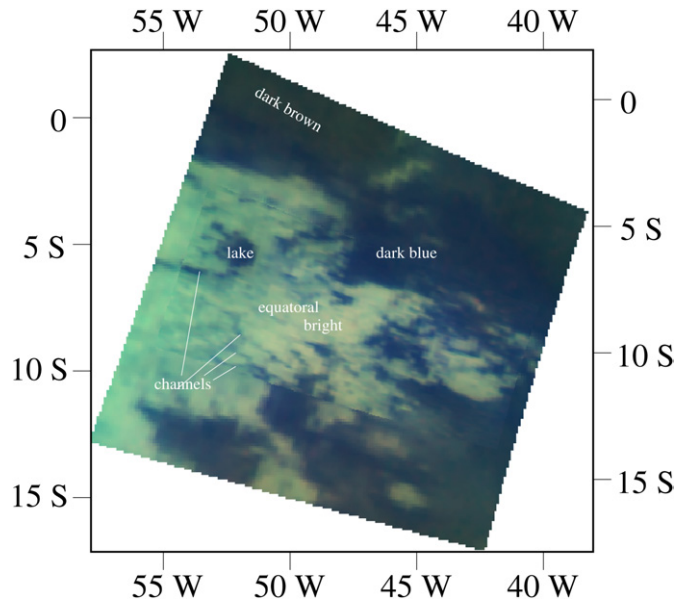


Fig. 11. T9 VIMS view of a bright peninsula east of Xanadu; maximum resolution is 3.7 km/pixel. The color scheme is the same as in Fig. 4, but we enhanced the contrast relative to the standard stretch to bright out detail in this particular area. Fensal dark area is at top, Aztlan dark area is at bottom. This is not the Huygens landing site, though it does have similar morphology and spectral unit distribution. The labeling of the ‘lake’ area is not meant to imply a body of liquid, but rather the output area of a drainage network that is probably presently dry.

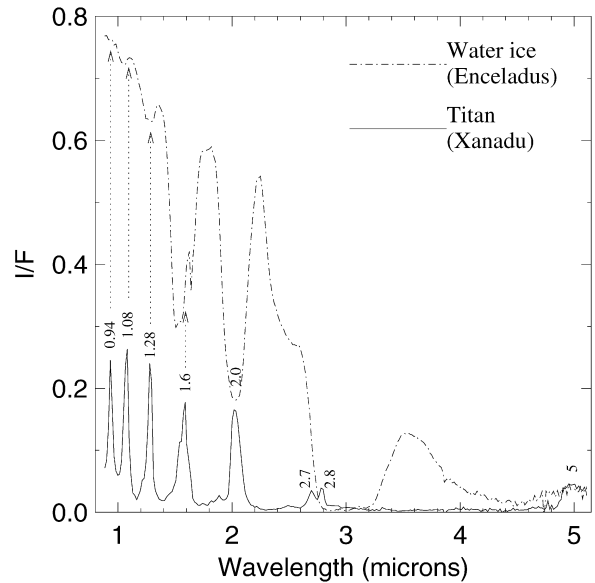


Fig. 12. Spectrum of Titan, with atmospheric windows labeled, compared to the spectrum of water ice that is actually a spectrum of Enceladus taken with VIMS. Enceladus’ surface is composed of nearly pure water ice (Brown et al., 2006). We interpret areas with relatively high 2.7/2.8  $\mu\text{m}$  ratios to possibly contain higher water ice concentrations, and those areas that are bright at 0.94, 1.08, and 1.28  $\mu\text{m}$  relative to 1.6, 2.0, and 5.0  $\mu\text{m}$  to possibly be more water ice rich as well.

#### 5.1.4. Equatorial bright

We term those non-Xanadu portions of the equatorial zone equatorial bright terrain. Dilmun, Quivira, and other unnamed bright areas such as the one shown in Fig. 11 fall into this category. The equatorial bright areas’ colors are ‘Xanadu lite’—

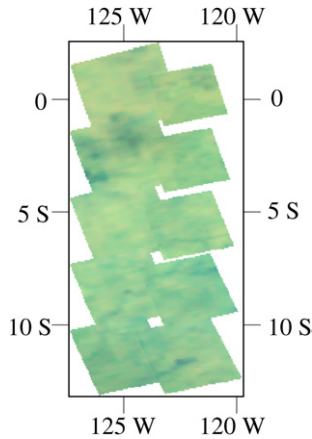


Fig. 13. VIMS Tb (2004 December 13) mosaic from central Xanadu. Colors are the same as in Fig. 4, contrast has been enhanced. Maximum resolution is 4.7 km/pixel.

bright but less so than Xanadu in the shorter wavebands, and still relatively dim at 5  $\mu\text{m}$ . The borders between equatorial bright and both dark units are sharp; the borders between equatorial bright and Xanadu are not.

As seen in Fig. 11, equatorial bright terrain shows numerous long, dark channels. Though there are some interior drainages, most of the channels are part of a large-scale integrated drainage network, implying that the equatorial bright terrain is old relative to the aggregate rainfall deposition rate. However, other areas at the same latitude must be at least somewhat dry in order to maintain active sand dunes. This seeming contradiction is consistent with the contention of Lorenz and Lunine (2005) that rainfall on Titan is infrequent but intense, as in the southwestern United States.

## 5.2. Mid-latitude zone

Titan's terrain in the mid-latitudes, from the edge of the equatorial zone near 25°–30° S to ~55° S in the southern hemisphere and from ~30° N at least to as close to the terminator as we can reliably see (see Fig. 9), is different in character from the equatorial zone. In particular, it is more highly reflective at 5  $\mu\text{m}$  than either the equatorial or south polar zones. None of the four units previously discussed extend into this zone. In general the area is brighter at 5  $\mu\text{m}$  than equatorial bright areas and includes one large bright region, Tsegih, and two smaller 5- $\mu\text{m}$ -bright regions enveloped by bright blue terrain. The border between the mid-latitude zone and the equatorial zone is somewhat fuzzy, with the transition taking place over a few hundred km.

### 5.2.1. Tsegih

Tsegih is a continent-sized area centered near 40° S 40° W that dominates Titan's sub-saturnian hemisphere. It is relatively bright at all wavelengths, though less so than Xanadu at all wavelengths except 5.0  $\mu\text{m}$ , and less so than the much smaller 5- $\mu\text{m}$ -bright areas. The boundaries of Tsegih are not sharp. Two prominent darker regions within Tsegih, located

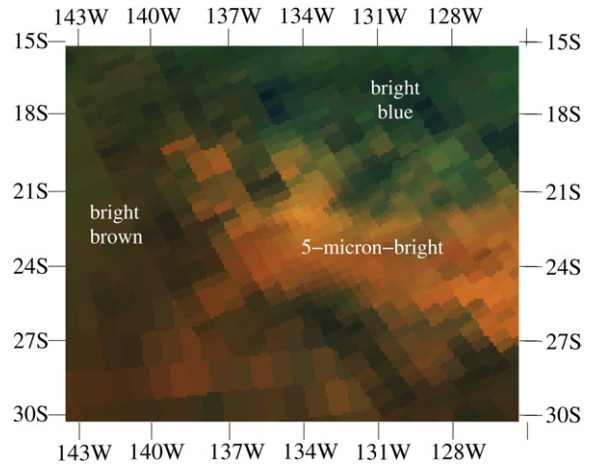


Fig. 14. VIMS Tb (2004 December 13) view of western Tui Regio, from Barnes et al. (2006). Colors are the same as in Fig. 4, contrast has been enhanced. Maximum resolution is 14 km/pixel.

near 40° W 35° S and 55° W 48° S, share the spectral signature of the adjacent south polar unit.

VIMS has not acquired any high-resolution coverage of Tsegih. What we do have shows a landscape that is moderately variable at the 100-km scale. While there is a single, large, channel-like feature between the two darker areas mentioned above, higher resolution coverage would be necessary to identify the presence or absence of channels like those seen in Fig. 11 for the equatorial bright terrain.

### 5.2.2. Bright brown

Most of the rest of the middle south latitudes that VIMS has seen so far are located on Titan's anti-Saturn hemisphere in the area south of Shangri-La and Xanadu. This unit, which we call bright brown, is characterized by reflectivities in-between that of the equatorial dark units and the equatorial bright unit at wavelengths shorter than 5  $\mu\text{m}$ . At longer wavelengths the bright brown unit exhibits a relatively red slope when compared to the rest of Titan's surface; it is as bright as Xanadu at 5  $\mu\text{m}$ .

VIMS' coverage of this unit to date has been at modest resolution (~10 km/pixel)—too low to test for the presence or absence of channels. Its spectrum is similar to the least bright parts of the 5- $\mu\text{m}$ -bright Tui Regio, which may imply an evolutionary relationship (Barnes et al., 2006).

### 5.2.3. 5- $\mu\text{m}$ -bright

There are two 5- $\mu\text{m}$ -bright regions located on the border between the mid-latitude zone and the equatorial zone south of Xanadu: Tui Regio, and "Hotei Regio." They are smaller in areal extent than the previously discussed units. The 5- $\mu\text{m}$ -bright regions were first discovered by VIMS, and determined to be surface features (Barnes et al., 2005). These regions are the brightest on Titan at all wavelengths, and 30% more reflective than anything else yet seen at 5  $\mu\text{m}$ .

High resolution views from both VIMS (see Fig. 14) and ISS show no channel-like features within the areas VIMS sees as 5- $\mu\text{m}$ -bright, implying that the surfaces in this unit are relatively young (Barnes et al., 2006). The 5- $\mu\text{m}$ -bright unit shows evi-

dence of flow features, possibly of extrusive origin (Barnes et al., 2006).

The composition that leads to higher 5  $\mu\text{m}$  reflectivities is not clear. However, 2.8/2.7  $\mu\text{m}$  band ratios show that the 5- $\mu\text{m}$ -bright is also highly reflective at 2.8  $\mu\text{m}$  relative to the rest of Titan (see Fig. 7). Thus the 5- $\mu\text{m}$ -bright unit may contain less water ice in its surface layer than the rest of Titan, as water has a strong absorption extending longward from  $\sim 2.7$   $\mu\text{m}$ .

#### 5.2.4. Bright blue

A bright blue spectral unit extends outward and eastward from Tui Regio, past “Hotei Regio,” and to the western margin of Aztlan. This unit is most visible in Figs. 6 and 7, and represents the most subtle unit designation we make in this work. It overlies ISS bright terrain—the blue spectral slope leads this unit to appear brighter in ISS images than in the longer wavelength VIMS windows.

Based on the morphology and color gradations in western Tui Regio and the bright blue unit’s association with 5- $\mu\text{m}$ -bright terrain, Barnes et al. (2006) suggested that this unit may represent an airfall deposit. The maps in Figs. 6 and 7 show that, in the areas covered to date, the bright blue unit occurs only in this area east and within  $10^\circ$  in latitude of Tui Regio.

In the 2.8/2.7  $\mu\text{m}$  ratio this unit shows unusually low 2.8  $\mu\text{m}$  reflectivity, and the unit also displays high reflectivity at 0.94, 1.08, and 1.28  $\mu\text{m}$  relative to 1.6, 2.0, and 5  $\mu\text{m}$ . Both conditions are consistent with a greater fraction of water ice within the bright blue unit relative to Titan’s average.

#### 5.3. South polar zone

Southward of  $55^\circ$ – $60^\circ$  S is a final spectral unit, the south polar unit. It is characterized by a gray relative spectral slope and moderately dark albedos. The margin of the south polar unit, while distinct, is not sharp. The nature of the boundary, smooth and parallel to lines of latitude, is consistent with the south polar zone being governed by thermal and/or atmospheric changes at  $55^\circ$ – $60^\circ$  S.

The geometry of *Cassini*’s flybys to date have limited VIMS’ resolution at the south pole to poorer than 50 km/pixel. No determination of the presence or absence of channels is possible. No high-resolution optical remote sensing coverage of Titan’s south pole is scheduled for the duration of *Cassini*’s primary mission.

## 6. Conclusions

VIMS’ 64-color near-global maps of Titan’s surface presented here represent an improvement greater than five-fold in spatial resolution over ground-based observations, while achieving better spectral resolution and coverage in 7 near-infrared spectral windows simultaneously. The maps’ coverage at  $\sim 50$  km/pixel is good between  $210^\circ$  W through the anti-Saturn point and around to  $330^\circ$  W south of  $60^\circ$  N. VIMS will obtain better coverage of Titan’s trailing hemisphere and north pole, as well as those south polar areas covered in cloud on T8 and T9, on future flybys.

Our maps show a latitudinal zonation in Titan’s spectral character. Though broadband color variations need not necessarily be meaningful compositionally, we identify those variations that exist. Near the equator we identify four spectral units, two dark and two bright; in the mid-south latitudes four more, two with large areal extent and two smaller; and southward of  $60^\circ$  S we identify a final spectral unit. We will present a quantitative map of each unit’s areal extent and a measure of each unit’s average spectrum in a future paper.

The mechanisms driving the latitudinal zonation that we see are not yet clear. Lorenz et al. (2006) suggest that the net transport direction via tidally-driven winds of sand particles concentrates them near the equator. This explanation is consistent with the extent of our dark brown unit, which corresponds to RADAR’s dune fields (Soderblom, in preparation) and does not extend beyond  $35^\circ$  from the equator. The concentration of dark blue near the equator may be related to its correlation with dark brown terrain.

The red slope and correspondingly high 5  $\mu\text{m}$  reflectivities that we see in the mid-southern latitudes relative to Xanadu and equatorial bright terrain cry out for explanation. This latitudinal difference could be thermal or atmospheric in source. Titan’s  $\sim 5$  K equator-to-pole temperature difference (Flasar et al., 2005) could be driving volatile species away from the equator to higher-latitude cold traps. This explanation may, however, be better suited to the formation of the south polar unit in that the pole should provide the best cold trap for volatiles, if there is one.

Alternatively, organic atmospheric haze with a red spectral slope could be washed from the surface preferentially at equatorial latitudes, or be precipitating from the atmosphere preferentially at mid-latitudes. No clouds have yet been observed at Titan’s equator, but storms have been seen repeatedly near  $40^\circ$  S (Griffith et al., 2005; Roe et al., 2005). Though we have only been able to spot clouds on Titan for much less than a full saturnian orbit, the data so far do not support preferential rain at the equator relative to mid-southern latitudes.

Recent theoretical models of Titan’s atmospheric circulation (Rannou et al., 2006) predict that rain and haze should concentrate near  $40^\circ$  latitude in both hemispheres. The presence of a south polar haze collar, as recently observed (Jackson et al., in preparation), supports these predictions. The situation in the mid-northern latitudes is not yet clear, but these areas do show some 5  $\mu\text{m}$  enhancement relative to the equatorial regions, similar to that seen in the mid-southern latitudes. If this symmetry holds up, then the 5  $\mu\text{m}$  enhancement would not likely be the result of wind-blown emissions from surface vents [whose existence is suggested by Roe et al. (2005)], but may rather result from non-isotropic deposition of haze particulate organic material.

Future VIMS global maps of Titan will allow for higher resolution, up to 45 pixels per degree, or about 1 km/pixel at the equator—better for sub-global regions. They will also support full 256-color mapping to include the VIMS channels where haze predominates over surface features. Geometric accuracy of the maps in the present work is probably no better than  $1^\circ$ – $3^\circ$ ; we are working on a system to register our observa-

tions to within  $\sim 0.05^\circ$  using our highest-resolution cubes and RADAR data. A final goal, to be completed a few years after the mission ends, is to produce atmospherically-corrected, global, best-resolution and best-S/N VIMS maps from all of *Cassini's* flybys.

## Acknowledgments

The authors thank the VIMS support team, Robert Watson, Dyer Lytle, Dan Moynihan, John Ivens, and Virginia Pasek, for their years of effort helping to bring VIMS' views of Titan home to Earth.

## References

- Acton, C.H., 1999. SPICE products available to the Planetary Science Community. *Lunar Planet. Sci.* 30, 1233–1234.
- Barnes, J.W., Brown, R.H., Turtle, E.P., McEwen, A.S., Lorenz, R.D., Janssen, M., Schaller, E.L., Brown, M.E., Buratti, B.J., Sotin, C., Griffith, C., Clark, R., Perry, J., Fussner, S., Barbara, J., West, R., Elachi, C., Bouchez, A.H., Roe, H.G., Baines, K.H., Bellucci, G., Bibring, J.-P., Capaccioni, F., Cerroni, P., Combes, M., Coradini, A., Cruikshank, D.P., Drossart, P., Formisano, V., Jaumann, R., Langevin, Y., Matson, D.L., McCord, T.B., Nicholson, P.D., Sicardy, B., 2005. A 5-micron-bright spot on Titan: Evidence for surface diversity. *Science* 310, 92–95.
- Barnes, J.W., Brown, R.H., Radebaugh, J., Buratti, B.J., Sotin, C., Le Mouélic, S., Rodriguez, S., Turtle, E.P., Perry, J., Clark, R., Baines, K.H., Nicholson, P.D., 2006. Cassini observations of flow-like features in western Tui Regio, Titan. *Geophys. Res. Lett.* 33, doi:10.1029/2006GL026843. L16204.
- Brown, R.H., Baines, K.H., Bellucci, G., Bibring, J.-P., Buratti, B.J., Capaccioni, F., Cerroni, P., Clark, R.N., Coradini, A., Cruikshank, D.P., Drossart, P., Formisano, V., Jaumann, R., Langevin, Y., Matson, D.L., McCord, T.B., Mennella, V., Miller, E., Nelson, R.M., Nicholson, P.D., Sicardy, B., Sotin, C., 2004. The Cassini Visual and Infrared Mapping Spectrometer (VIMS) investigation. *Space Sci. Rev.* 115, 111–168.
- Brown, R.H., Clark, R.N., Buratti, B.J., Cruikshank, D.P., Barnes, J.W., Mastropa, R.M.E., Bauer, J., Newman, S., Momary, T., Baines, K.H., Bellucci, G., Capaccioni, F., Cerroni, P., Combes, M., Coradini, A., Drossart, P., Formisano, V., Jaumann, R., Langevin, Y., Matson, D.L., McCord, T.B., Nelson, R.M., Nicholson, P.D., Sicardy, B., Sotin, C., 2006. Composition and physical properties of Enceladus' surface. *Science* 311, 1425–1428.
- Capaccioni, F., Coradini, A., Cerroni, P., Amici, S., 1998. Imaging spectroscopy of Saturn and its satellites: VIMS-V onboard Cassini. *Planet. Space Sci.* 46, 1263–1276.
- Combes, M., Vapillon, L., Gendron, E., Coustenis, A., Lai, O., Witteberg, R., Sirdey, R., 1997. Spatially resolved images of Titan by means of adaptive optics. *Icarus* 129, 482–497.
- Coustenis, A., Lellouch, E., Maillard, J.P., McKay, C.P., 1995. Titan's surface: Composition and variability from the near-infrared albedo. *Icarus* 118, 87–104.
- Coustenis, A., Gendron, E., Lai, O., Véran, J.-P., Woillez, J., Combes, M., Vapillon, L., Fusco, T., Mugnier, L., Rannou, P., 2001. Images of Titan at 1.3 and 1.6  $\mu\text{m}$  with adaptive optics at the CFHT. *Icarus* 154, 501–515.
- Coustenis, A., Hirtzig, M., Gendron, E., Drossart, P., Lai, O., Combes, M., Negrão, A., 2005. Maps of Titan's surface from 1 to 2.5  $\mu\text{m}$ . *Icarus* 177, 89–105.
- Elachi, C., Wall, S., Allison, M., Anderson, Y., Boehmer, R., Callahan, P., Encrenaz, P., Flamini, E., Franceschetti, G., Gim, Y., Hamilton, G., Hensley, S., Janssen, M., Johnson, W., Kelleher, K., Kirk, R., Lopes, R., Lorenz, R., Lunine, J., Muhleman, D., Ostro, S., Paganelli, F., Picardi, G., Posa, F., Roth, L., Seu, R., Shaffer, S., Soderblom, L., Stiles, B., Stofan, E., Vetrilla, S., West, R., Wood, C., Wye, L., Zebker, H., 2005. Cassini radar views the surface of Titan. *Science* 308 (5724), 970–974.
- Elachi, C., Wall, S., Janssen, M., Stofan, E., Lopes, R., Kirk, R., Lorenz, R., Lunine, J., Paganelli, F., Soderblom, L., Wood, C., Wye, L., Zebker, H., Anderson, Y., Ostro, S., Allison, M., Boehmer, R., Callahan, P., Encrenaz, P., Flamini, E., Franceschetti, G., Gim, Y., Hamilton, G., Hensley, S., Johnson, W., Kelleher, K., Muhleman, D., Picardi, G., Posa, F., Roth, L., Seu, R., Shaffer, S., Stiles, B., Vetrilla, S., West, R., 2006. Titan radar mapper observations from Cassini's T3 fly-by. *Nature* 441, 709–713.
- Flasar, F.M., Achterberg, R.K., Conrath, B.J., Gierasch, P.J., Kunde, V.G., Nixon, C.A., Bjoraker, G.L., Jennings, D.E., Romani, P.N., Simon-Miller, A.A., Bézard, B., Coustenis, A., Irwin, P.G.J., Teanby, N.A., Brasunas, J., Pearl, J.C., Segura, M.E., Carlson, R.C., Mamoutkine, A., Schinder, P.J., Barucci, A., Courtin, R., Fouchet, T., Gautier, D., Lellouch, E., Marten, A., Prangé, R., Vinatier, S., Strobel, D.F., Calcutt, S.B., Read, P.L., Taylor, F.W., Bowles, N., Samuelson, R.E., Orton, G.S., Spilker, L.J., Owen, T.C., Spencer, J.R., Showalter, M.R., Ferrari, C., Abbas, M.M., Raulin, F., Edgington, S., Ade, P., Wishnow, E.H., 2005. Titan's atmospheric temperatures, winds, and composition. *Science* 308, 975–978.
- Gendron, E., Coustenis, A., Drossart, P., Combes, M., Hirtzig, M., Lacombe, F., Rouan, D., Collin, C., Pau, S., Lagrange, A.-M., Mouillet, D., Rabou, P., Fusco, T., Zins, G., 2004. VLT/NACO adaptive optics imaging of Titan. *Astron. Astrophys.* 417, L21–L24.
- Gibbard, S.G., Macintosh, B., Gavel, D., Max, C.E., de Pater, I., Ghez, A.M., Young, E.F., McKay, C.P., 1999. Titan: High-resolution speckle images from the Keck telescope. *Icarus* 139, 189–201.
- Gibbard, S.G., de Pater, I., Macintosh, B.A., Roe, H.G., Max, C.E., Young, E.F., McKay, C.P., 2004. Titan's 2  $\mu\text{m}$  surface albedo and haze optical depth in 1996–2004. *Geophys. Res. Lett.* 31, 17.
- Griffith, C.A., 1993. Evidence for surface heterogeneity on Titan. *Nature* 364, 511–514.
- Griffith, C.A., Pentead, P., Baines, K., Drossart, P., Barnes, J., Bellucci, G., Bibring, J., Brown, R., Buratti, B., Capaccioni, F., Cerroni, P., Clark, R., Combes, M., Coradini, A., Cruikshank, D., Formisano, V., Jaumann, R., Langevin, Y., Matson, D., McCord, T., Mennella, V., Nelson, R., Nicholson, P., Sicardy, B., Sotin, C., Soderblom, L.A., Kursinski, R., 2005. The evolution of Titan's mid-latitude clouds. *Science* 310, 474–477.
- Hoppa, G.V., Tufts, B.R., Greenberg, R., Geissler, P.E., 1999. Formation of cycloidal features on Europa. *Science* 285, 1899–1902.
- Jaumann, R., Stephan, K., Brown, R.H., McCord, T.B., Coradini, A., Capaccioni, F., Filacchione, G., Clark, R.N., Cerroni, P., Baines, K.H., Bellucci, G., Bibring, J.-P., Buratti, B.J., Bussolotti, E., Combes, M., Cruikshank, D.P., Drossart, P., Formisano, V., Langevin, Y., Matson, D.L., Nelson, R.M., Nicholson, P.D., Sicardy, B., Sotin, C., Roatsch, T., Scholten, F., Matz, K.-D., 2006. High resolution Cassini-VIMS mosaics of Titan and the icy saturnian satellites. *Planet. Space Sci.*, doi:10.1016/j.pss.2006.05.034. In press.
- Lemmon, M.T., Karkoschka, E., Tomasko, M., 1993. Titan's rotation—Surface feature observed. *Icarus* 103, 329–332.
- Lorenz, R.D., Lunine, J.I., 2005. Titan's surface before Cassini. *Planet. Space Sci.* 53, 557–576.
- Lorenz, R.D., Wall, S., Radebaugh, J., Boubin, G., Reffet, E., Janssen, M., Stofan, E., Lopes, R., Kirk, R., Elachi, C., Lunine, J., Mitchell, K., Paganelli, F., Soderblom, L., Wood, C., Wye, L., Zebker, H., Anderson, Y., Ostro, S., Allison, M., Boehmer, R., Callahan, P., Encrenaz, P., Ori, G.G., Franceschetti, G., Gim, Y., Hamilton, G., Hensley, S., Johnson, W., Kelleher, K., Muhleman, D., Picardi, G., Posa, F., Roth, L., Seu, R., Shaffer, S., Stiles, B., Vetrilla, S., Flamini, E., West, R., 2006. The sand seas of Titan: Cassini RADAR observations of longitudinal dunes. *Science* 312, 724–727.
- McCord, T. B., Hansen, G. B., Buratti, B. J., Clark, R. N., Cruikshank, D. P., D'Aversa, E., Griffith, C. A., 2006. Composition of Titan's surface from Cassini VIMS. *Planet. Space Sci.*, doi:10.1016/j.pss.2006.06.007. In press.
- Meier, R., Smith, B.A., Owen, T.C., Terrile, R.J., 2000. The surface of Titan from NICMOS observations with the Hubble Space Telescope. *Icarus* 145, 462–473.
- Noll, K.S., Geballe, T.R., Knacke, R.F., Pendleton, Y.J., 1996. Titan's 5  $\mu\text{m}$  spectral window: Carbon monoxide and the albedo of the surface. *Icarus* 124, 625–631.
- Owen, T.C., Aksnes, K., Beebe, R., Blue, J., Brahic, A., Burba, G.A., Smith, B.A., Tejfel, V.G., 2006. Titan: Nomenclature system and the very first names for one more world. *Lunar Planet. Sci.* 37, 1082–1083.

- Porco, C.C., Baker, E., Barbara, J., Beurle, K., Brahic, A., Burns, J.A., Charnoz, S., Cooper, N., Dawson, D.D., Del Genio, A.D., Denk, T., Dones, L., Dyudina, U., Evans, M.W., Fussner, S., Giese, B., Grazier, K., Helfenstein, P., Ingersoll, A.P., Jacobson, R.A., Johnson, T.V., McEwen, A., Murray, C.D., Neukum, G., Owen, W.M., Perry, J., Roatsch, T., Spitale, J., Squyres, S., Thomas, P., Tiscareno, M., Turtle, E.P., Vasavada, A.R., Veverka, J., Wagner, R., West, R., 2005. Imaging of Titan from the Cassini spacecraft. *Nature* 434, 159–168.
- Rannou, P., Montmessin, F., Hourdin, F., Lebonnois, S., 2006. The latitudinal distribution of clouds on Titan. *Science* 311, 201–205.
- Richardson, J., Lorenz, R.D., McEwen, A., 2004. Titan's surface and rotation: New results from Voyager 1 images. *Icarus* 170, 113–124.
- Rodriguez, S., Le Mouèlic, S., Sotin, C., Clenet, H., Clark, R. N., Buratti, B. J., Brown, R. H., McCord, T. B., and the VIMS Science Team, 2006. Cassini/VIMS hyperspectral observations of the Huygens landing site on Titan. *Planet. Space Sci.*, doi:10.1016/j.pss.2006.06.016. In press.
- Roe, H.G., de Pater, I., Gibbard, S.G., Macintosh, B.A., Max, C.E., Young, E.F., Brown, M.E., Bouchez, A.H., 2004. A new 1.6-micron map of Titan's surface. *Geophys. Res. Lett.* 31, 17–20.
- Roe, H.G., Brown, M.E., Schaller, E.L., Bouchez, A.H., Trujillo, C.A., 2005. Geographic control of Titan's mid-latitude clouds. *Science* 310, 477–479.
- Smith, P.H., Lemmon, M.T., Lorenz, R.D., Stromovsky, L.A., Caldwell, J.J., Allison, M.D., 1996. Titan's surface, revealed by HST Imaging. *Icarus* 119, 336–349.
- Sotin, C., Jaumann, R., Buratti, B.J., Brown, R.H., Clark, R.N., Soderblom, L.A., Baines, K.H., Bellucci, G., Bibring, J.-P., Capaccioni, F., Cerroni, P., Combes, M., Coradini, A., Cruikshank, D.P., Drossart, P., Formisano, V., Langevin, Y., Matson, D.L., McCord, T.B., Nelson, R.M., Nicholson, P.D., Sicardy, B., Le Mouèlic, S., Rodriguez, S., Stephan, K., Scholz, C.K., 2005. Release of volatiles from a possible cryovolcano from near-infrared imaging of Titan. *Nature* 435, 786–789.
- Thekekar, M.P., 1973. Solar energy outside the Earth's atmosphere. *Sol. Energy* 14, 109–127.
- Tomasko, M.G., Archinal, B., Becker, T., Bézard, B., Bushroo, M., Combes, M., Cook, D., Coustenis, A., de Bergh, C., Dafoe, L.E., Doose, L., Douté, S., Eibl, A., Engel, S., Gliem, F., Grieger, B., Holso, K., Howington-Kraus, E., Karkoschka, E., Keller, H.U., Kirk, R., Kramm, R., Küppers, M., Lanagan, P., Lellouch, E., Lemmon, M., Lunine, J., McFarlane, E., Moores, J., Prout, G.M., Rizk, B., Rosiek, M., Rueffer, P., Schröder, S.E., Schmitt, B., See, C., Smith, P., Soderblom, L., Thomas, N., West, R., 2005. Rain, winds and haze during the Huygens probe's descent to Titan's surface. *Nature* 438, 765–778.